The Dense Plasma Torus around the Nucleus of an Active Galaxy NGC 1052

Seiji Kameno, Satoko Sawada-Satoh, Makoto Inoue,
Zhi-Qiang Shen, and Kiyoaki Wajima

To appear in
Publications of the Astronomical Society of Japan
Vol. 53, No.2, 2001

The dense plasma torus around the nucleus of an active galaxy NGC 1052

Seiji Kameno,[1] Satoko Sawada-Satoh,[1,2] Makoto Inoue,[1] Zhi-Qiang Shen,[2] and Kiyoaki Wajima[2]

[1] *National Astronomical Observatory, 2-21-1 Osawa, Mitaka, Tokyo 181-8588*

E-mail(SK): kameno@hotaka.mtk.nao.ac.jp

[2] *The Institute of Space and Astronautical Science, 3-1-1 Yoshinodai, Sagamihara, Kanagawa 229-8510*

(Received 2000 December 27; accepted 2001 February 9)

Abstract

A subparsec-scale dense plasma torus around an active galactic nucleus (AGN) is unveiled. We report very-long-baseline interferometry (VLBI) observations at 2.3, 8.4, and 15.4 GHz towards the active galaxy NGC 1052. Convex spectra of the double-sided jets and the nucleus imply that synchrotron emission is obscured through the free–free absorption (FFA) by the foreground cold dense plasma. A trichromatic image was produced to illustrate distribution of the FFA opacity. We found a central condensation of the plasma which covers about 0.1 pc and 0.7 pc of the approaching and receding jets, respectively. A simple explanation for the asymmetric distribution is the existence of a thick plasma torus perpendicular to the jets. We also found an ambient FFA absorber, whose density profile can be ascribed to a spherical distribution of the isothermal King model. Coexistence of torus-like and spherical distributions of the plasma suggests a transition from the radial accretion to the rotational accretion around the nucleus.

Key words: galaxies: active — galaxies: nuclei — galaxies: individual (NGC 1052, 0238 − 084) — radio continuum: galaxies — techniques: interferometric

1. Introduction

The giant elliptical galaxy NGC 1052, which is also classified as a low-ionization nuclear emission-line region (LINER) galaxy, holds an AGN in the center (Ho et al. 1997). If we assume $H_0 = 75$ km s^{-1} Mpc^{-1} and $q_0 = 0.5$, the redshift $z = 0.0049$ (Knapp et al. 1978) corresponds to the distance of 20 Mpc, and 1 milliarcsec (mas) corresponds to 0.095 pc. At radio wavelengths, double-sided jets elongated by several pc in P.A.$\sim 65°$ are seen with an emission gap in between (Claussen et al. 1998; Kellermann et al. 1998), though it is unclear where the nucleus is. Water masers are found along the jet, which are considered to be excited by shocks into circumnuclear molecular clouds, or amplification of the radio continuum emission of the jet by foreground molecular clouds (Claussen et al. 1998). This object shows a convex radio spectrum peaked at 10 GHz, to be classified as a GHz-Peaked Spectrum (GPS) source (O'Dea 1998; de Vries et al. 1997). A steep spectrum with $\alpha_0 = -1.33$ ($S_\nu \propto \nu^{+\alpha_0}$) at frequencies above the peak (de Vries et al. 1997) and high brightness temperature of $\sim 10^9$ K (see section 3.1) indicate synchrotron radiation.

Two possible hypotheses are proposed for the rising spectrum below the peak frequency in GPS sources; synchrotron self-absorption (SSA) or free–free absorption (FFA). Both can generate convex spectra; $S_\nu \propto \nu^{2.5}\left[1 - \exp(-\tau_{\rm s}\nu^{\alpha_0 - 2.5})\right]$ for SSA, and $S_\nu \propto \nu^{\alpha_0}\exp(-\tau_{\rm f}\nu^{-2.1})$ for FFA, where ν is the frequency in GHz, $\tau_{\rm s}$ and $\tau_{\rm f}$ are the SSA and FFA coefficients, respectively, and α_0 is the intrinsic spectral index. In general, a spectral shape will be a product of both. FFA arises from an external absorber in front of the synchrotron emitter, while SSA is an internal process of the synchrotron emission via interaction between relativistic plasma and magnetic field. These spectral shapes resemble each other, so that precise spectral measurements are necessary to detect small difference. FFA can generate steeper cutoff than the maximum attainable spectral index α of 2.5 by SSA. Thus, a component with $\alpha > 2.5$ could be an evidence of FFA. Another distinction is related to difference of the peak frequencies in twin jets. In case of SSA, the peak frequency in the receding jet should be lower than that in the approaching jet due to the Doppler shift, if we assume an intrinsic symmetry. On the contrary, longer path length towards the receding jet causes the deeper FFA opacity and then the higher peak frequency. A sufficiently high spatial resolution is crucial to avoid spectral blending, as demonstrated by Kameno et al. (2000).

The FFA coefficient is related to the electron density $n_{\rm e}$ (cm^{-3}) and electron temperature $T_{\rm e}$ (K) by

$$\tau_{\rm f} = 0.46 \int_{\rm LOS} n_{\rm e}^2 T_{\rm e}^{-3/2} dL, \tag{1}$$

where $\int_{\rm LOS} dL$ is the integration via the line of sight in pc, so that it can be a probe for cold dense plasma (Pacholczyk 1970).

There exist increasing evidences for FFA towards active galaxies. One remarkable milestone is the discovery of a counter-jet in 3C 84 at the center of the nearby Seyfert/cD galaxy NGC 1275 (Vermeulen et al. 1994; Walker et al. 1994). The counter-jet showed a strongly inverted spectrum unlike the approaching jet with a steep spectrum, whose feature can be explained by free–free absorption (FFA) due to ambient cold dense plasma (see the Appendix). The idea was confirmed by following VLBA observations by Walker et al. (2000) and VSOP observations by Asada et al. (2000).

FFA towards GPS sources was predicted by Bicknell et al. (1997). They suggested that photoionization of the interstellar medium (ISM) by the radiative shocks produces the ionized gas, which has a significant emission measure and a correspondingly high FFA opacity. Discovery of FFA towards GPS sources was made by the space-VLBI observation towards a GPS galaxy OQ 208, which showed convex spectra towards two radio lobes separated by 10 pc. Difference in the path length along the line of sight between two lobes causes an asymmetry in FFA opacity, with a larger opacity towards the far-side lobe. The FFA opacity implied that cold ($T_{\rm e} \sim 10^5$ K) dense ($n_{\rm e} \sim 10^5$ cm^{-3}) plasma associates with the central tens of pc (Kameno et al. 2000). This result showed that multi-frequency VLBI observations are crucial to clarify the FFA, which can be a probe of the matter in the vicinity of AGN. The discovery of the FFA absorber is followed by observations towards the radio galaxies NGC 4261 (Jones et al. 2000) and 0108+388 (Marr et al. 2000).

We prospect two advantages for the FFA as a probe of an accreting matter, when the absorber covers the background bright core and jets. First, since the absorber must be at the near side of the jet, it allows us to figure a 3-dimensional geometry of the system. Second, the opacity provides physical properties of the absorber such as the electron density $n_{\rm e}$ and the temperature $T_{\rm e}$. NGC 1052, the nearest GPS source showing the double-sided jets, is one of the best target sources.

In this paper, we report simultaneous trichromatic Very Long Baseline Array (VLBA) observations towards NGC 1052 at 2.3, 8.4, and 15.4 GHz that produce an FFA opacity map. Our aim is to investigate the geometry and physical properties of the FFA absorber.

2. Observations and Data Reduction

Using the VLBA of the National Radio Astronomy Observatory (NRAO), we observed NGC 1052 at three frequencies (2.3, 8.4, and 15.4 GHz) simultaneously on 15 December 1998. The subreflector switched between the dual-frequency 2.3/8.4 GHz reflector system and the 15.4 GHz feed horn with a 22-min cycle. We used 4 channels of 8 MHz bandwidth at 15.4 GHz, and allocated 2 channels at both 2.3 and 8.4 GHz. The correlation process was accomplished by the VLBA correlator. We applied fringe-fitting, data flagging, and a priori amplitude calibration in the NRAO AIPS. Imaging and self-calibration processes were carried out by Difmap. We took uniform weighting with scaling by errors raised to the power -1. Synthesized beam sizes (FWHM) were 6.06×2.45 mas in P.A.$= 3^\circ.92$, 2.01×0.78 mas in P.A.$= -1^\circ.91$, and 1.03×0.40 mas in P.A.$= -2^\circ.53$, for 2.3, 8.4, and 15.4 GHz, respectively.

While relative gain errors among the antennae are corrected though amplitude self-calibration processes, further flux calibration is necessary to obtain certain spectra across the observing frequencies. For the purpose of absolute flux calibration, we also imaged four calibrators; the BL Lacertae, DA 193, 3C 279, and OT 081. Basing on the comparison between the total flux measurements by the University of Michigan Radio Astronomy Observatory (UMRAO) and the NRAO Green Bank interferometer, and summation of CLEANed flux densities, we applied flux scaling for the final results. At 15.4 GHz, for instance, total CLEANed flux densities before absolute correction were 3.276, 5.012, 25.769, and 4.172 Jy for BL Lac, DA 193, 3C 279, and OT 081, respectively. The UMRAO database provides the total flux densities at 14.5 GHz, 3.458 ± 0.015, 4.763 ± 0.035, 27.69 ± 0.18, and 4.380 ± 0.030 Jy for each, as averaged over 2 months centered at our observation. Then we calculated a correction factor ($= \frac{\text{total CLEANed flux density}}{\text{UMRAO flux density}}$) of 0.959 ± 0.018, so that we scaled our image by the factor and obtained the accuracy of the flux scale of 1.8 %. The accuracy was derived from a standard deviation of the correction factors by the four calibrators. With the same manner, we scaled images at 2.3 and 8.4 GHz

by the correction factors of 0.84 and 0.79, respectively. The estimated amplitude accuracies are 4.0, 7.2 and 1.8 % at 2.3, 8.4, and 15.4 GHz, respectively. The images are shown in figure 1.

3. Discussion

3.1. Component Identification and Spectrum

For the purpose of registration, we pick up three distinct components A, B, and C (see figure 1). Using IMFIT in AIPS, we measure the relative positions, sizes and flux densities of these components, as listed in table 1. In advance of the IMFIT process, we restored the CLEAN images with a Gaussian beam of 3×1.5 mas in P.A.$= 0°$ to match the resolutions. Double-sided jet components A and C are identified with the similar separations of 9.5, 7.7, and 6.8 mas at 2.3, 8.4, and 15.4 GHz, respectively. An unresolved component B is clearly seen with a significant flux density of 489 ± 9 mJy at 15.4 GHz, but becomes fainter 77 ± 6 mJy at 8.4 GHz and too faint (< 5.6 mJy) to be identified at 2.3 GHz.

These components allow us to register three images to minimize the total difference of their positions. At any given frequency, we measured positions (ξ_k^ν, η_k^ν) of these three components relative to a tentative origin of each image, where k and ν stand for an index of components (A, B, and C) and a frequency, respectively. We then derived relative offsets $(\delta\xi^\nu, \delta\eta^\nu)$ between images to minimize the positional residuals χ_ν^2 defined as

$$\chi_\nu^2 = \sum_k \left[\frac{(\xi_k^\nu - \delta\xi^\nu - \xi_k^{\nu_0})^2}{\sigma_{\xi_k^\nu}^2 + \sigma_{\xi_k^\nu}^2} + \frac{(\eta_k^\nu - \delta\eta^\nu - \eta_k^{\nu_0})^2}{\sigma_{\eta_k^\nu}^2 + \sigma_{\eta_k^\nu}^2} \right], \tag{2}$$

where $\sigma_{\xi_k^\nu}$ and $\sigma_{\eta_k^\nu}$ are standard positional errors of component k at the frequency ν. The reference frequency ν_0 is put at 8.4 GHz. The r.m.s. errors of the registration in (ξ, ν) were $(0.25, 0.09)$ mas between 15.4 and 8.4 GHz, and $(0.20, 0.25)$ mas between 8.4 and 2.3 GHz, respectively. Response to the registration errors will be discussed in section 3.4.

Using the image registration, we synthesize a trichromatic image (figure 2) allocating red, green, blue channels for 2.3, 8.4, and 15.4 GHz, respectively, using the beam-matched images. Blue color covering component B and western ~ 5 mas indicates a steeply rising spectrum ($\alpha > 0$), while red color in the both ends of elongation shows $\alpha < 0$.

Figure 3 shows spectra of the components. Both A and C show convex spectra, which can be fitted by optically-thin synchrotron emission obscured by the cold plasma via thermal FFA. The spectral index $\alpha_0 = -1.33$ (de Vries et al. 1997) was too steep to fit, instead, we obtained $\alpha_0 = -0.65$ from the best fit. A and C mark the spectral peaks at 4.9 and 7.6 GHz, respectively, while B must have the peak above 15 GHz. Although the spectra of A and C seem similar, the difference of the peak frequencies is significant. The colors of these components in the trichromatic image (figure 2) emphasize the difference. Spectral indices between 2.3 and 8.4 GHz are $\alpha_{2.3}^{8.4} = 0.5 \pm 0.1$ and 2.3 ± 0.1 for A and C, and $\alpha_{2.3}^{8.4} > 2.0$ for B. Component B shows a large spectral index $\alpha_{8.4}^{15.4} = 3.1 \pm 0.1$ between 8.4 and 15.4 GHz. It exceeds the theoretical limit for SSA of 2.5 with a uniform magnetic field (Pacholczyk 1970). A and C are resolved at 15.4 GHz with the brightness temperatures $T_{\rm b} = (2.32 \pm 0.04) \times 10^9$ K and $(0.97 \pm 0.02) \times 10^9$ K, respectively, while component B is unresolved and shows the highest $T_{\rm b} > 1.48 \times 10^{10}$ K. Thus, we identify component B as the nucleus.

3.2. Viewing Angle of the Jet Axis

To clarify the geometry of the jet, we analyze the Doppler beaming effect (Blandford, Königl 1979; Pearson, Zensus 1987). Although both FFA and the Doppler beaming result in an apparent asymmetry of brightness between approaching and receding jets, the former is negligible at frequencies beyond the peak. If we assume intrinsic symmetry of the double-sided jets, the brightness ratio R is related to the intrinsic jet velocity β (in the unit of the speed of light) and the viewing angle θ by

$$R = \frac{T_{\rm b}^+}{T_{\rm b}^-} = \left(\frac{1+\beta\cos\theta}{1-\beta\cos\theta}\right)^{2-\alpha_0} . \tag{3}$$

Here, $T_{\rm b}^+$ and $T_{\rm b}^-$ are the brightness temperature of the approaching and receding jets, respectively. Substituting $T_{\rm b}^+ = (2.32 \pm 0.04) \times 10^9$ K and $T_{\rm b}^- = (0.97 \pm 0.02) \times 10^9$ K of components A and C, respectively, we have $R = 2.4 \pm 0.1$ at 15 GHz, and $\beta\cos\theta = 0.16 \pm 0.01$ for $\alpha_0 = -0.65$. Apparent proper motion of the jet gives another constraint. Relative proper motion of 1.3 mas yr^{-1} between the approaching and receding jets (Kellermann et al. 1999) corresponds to $\beta_{\rm app} = \beta_{\rm app}^+ + \beta_{\rm app}^- = 0.40$. Here, positive and negative signs are for approaching and receding jets, respectively. Using the formula of the

apparent velocity (Blandford, Königl 1979):

$$\beta_{\rm app}^{\pm} = \frac{\beta \sin\theta}{1 \mp \beta\cos\theta}, \tag{4}$$

then we have $\beta \sin\theta = \beta_{\rm app}(1-\beta^2\cos^2\theta)/2$. Finally, we obtain $\beta = 0.25$ and $\theta = 50°$. This is a rough estimation, nevertheless, it is obvious that the eastern and western jets are approaching and receding, respectively. The proper motion analysis based on the VLBA monitoring program at 15 GHz (Kellermann et al. 1998; Kellermann et al. 1999) will confirm these results and evaluate the accuracy.

3.3. The Absorption Mechanisms

We discuss about the origin of the low-frequency cutoff in the spectra; SSA or FFA. In the SSA process, the opacity is related to the magnetic field B and brightness temperature $T_{\rm b}$ at the peak frequency. If we assume equipartition between magnetic field and electrons, the peak frequency $\nu_{\rm m}$ in GHz is given by (Kellermann, Pauliny-Toth 1981)

$$\nu_{\rm m} \sim 8B^{1/5}S_{\rm m}^{2/5}\phi^{-4/5}(1+z)^{1/5}. \tag{5}$$

Here, the magnetic field B is in G, the peak flux density $S_{\rm m}$ is in Jy, the component size ϕ is in mas. Equation 5 is replaced by

$$B = 4.57 \times 10^{19}\nu_{\rm m}T_{\rm b}^{-2}(1+z), \tag{6}$$

using the brightness temperature of Gaussian component $T_{\rm b}$ in K,

$$T_{\rm b} = 1.224 \times 10^{12} S\nu^{-2}\phi^{-2}(1+z). \tag{7}$$

For the approaching jet component A, the peak flux density $S_{\rm m} = 2.0$ Jy and the size of $\phi = \sqrt{\phi_{\rm maj}\phi_{\rm min}} =$ 2 mas at the peak frequency $\nu_{\rm m} = 4.9$ GHz give $T_{\rm b} = 2.6 \times 10^{10}$ K. In the co-moving frame, the peak frequency is modified as $\nu_{\rm m}^* = 4.3$ GHz by the Doppler correction;

$$\nu_{\rm m}^* = \nu_{\rm m}(1+z)\frac{1-\beta\cos\theta}{\sqrt{1-\beta^2}}. \tag{8}$$

The brightness temperature in the co-moving frame $T_{\rm b}^*$ is also corrected by

$$T_{\rm b}^* = T_{\rm b}\left(\frac{1-\beta\cos\theta}{\sqrt{1-\beta^2}}\right)^{2-\alpha_0}, \tag{9}$$

and $T_{\rm b}^* = 1.5 \times 10^{10}$ K is obtained. Thus we have $B = 0.9$ G.

For the receding jet component C, we have $\nu_{\rm m} = 7.6$ GHz, $S_{\rm m} = 0.25$ Jy, $\phi = 1.0$ mas, and $T_{\rm b} = 5.3 \times 10^9$ K. These values should be corrected as

$$\nu_{\rm m}^* = \nu_{\rm m}(1+z)\frac{1+\beta\cos\theta}{\sqrt{1-\beta^2}}, \tag{10}$$

$$T_{\rm b}^* = T_{\rm b}\left(\frac{1+\beta\cos\theta}{\sqrt{1-\beta^2}}\right)^{2-\alpha_0}. \tag{11}$$

Thus, we have $\nu_{\rm m}^* = 9.2$ GHz, $T_{\rm b}^* = 8.6 \times 10^9$ K, and therefore $B = 5.7$ G. Such strong magnetic fields are unrealistic and impossible to sustain synchrotron emission for years against synchrotron loss. If we assume that component A and C have been emitting for 20 yr (= separation / apparent speed) without re-acceleration, $B < 55$ mG is required to sustain synchrotron emission with a break frequency $\nu_{\rm T} > 15.4$ GHz. In this case, $\nu_{\rm m} < 260$ MHz. Thus, the synchrotron emission is likely to be optically thin, in terms of SSA, towards the jets throughout our observing frequencies.

Since SSA is an internal process in the jet, difference of the peak frequencies at rest frame requires intrinsic asymmetry of the magnetic fields between the approaching and receding jets. On the contrary, FFA naturally generates higher peak frequency towards the receding jet than towards the approaching one. In case of spherically-symmetric distribution of the external absorber, the path length along the line of sight will be longer towards the receding jet than towards the approaching one. Furthermore, if the absorber forms a disk or a torus perpendicular to the jet, it covers the receding jet but does not the approaching jet. Such a geometry will be discussed in the next section.

Although $T_{\rm b}$ and $\nu_{\rm m}$ are uncertain for component B, implication for the magnetic field is possible. Since the total flux density of 1.02 ± 0.12 Jy at 31.4 GHz (Geldzahler, Witzel 1981) is less than a natural extension of the rising spectrum of component B, the peak frequency $\nu_{\rm m}$ should be 15.4 GHz $< \nu_{\rm m} <$ 31.4 GHz. The intrinsic brightness temperature should be less than the Compton limit $T_{\rm b} < 10^{12}$ K. Therefore, 7×10^{-4} G $< B <$ 7 G. Although the nucleus component B could be optically thick by SSA, its spectral index of $\alpha_{8.4}^{15.4} = 3.1 \pm 0.1$ requires a significant contribution of FFA. To keep simplicity, we later analyze the spectra assuming that the synchrotron emission is optically thin in terms of SSA, rather than a mixture of SSA and FFA. Our FFA analysis would be modified if SSA opacity were revealed by future

observations.

In some GPS sources, the SSA model outputs acceptable strength of the magnetic fields. Mutel et al. (1985) calculated magnetic fields of $\sim 10^{-4} - 10^{-3}$ G from SSA for three sources 1518+047, CTD 93, and 2050+364. Readhead et al. (1996) estimated the magnetic fields of $3 \times 10^{-2} h^{2/7}$ G and $4 \times 10^{-2} h^{2/7}$ for bright jet components B_1 and B_2 of a GPS source 2352+495, based on the brightness temperatures of $T_{\rm b} = 2 \times 10^{10}$ K and 2×10^{11} K, and the peak frequency of $\nu_{\rm m} \sim 1.66$ GHz, with the Hubble constant $H_0 = 100h$ km s^{-1} Mpc^{-1}. Shaffer et al. (1999) derived $B = 10^{-4}$ G for the lobes of a GPS source CTD 93 based on $T_{\rm b} = 1.3 \times 10^{11}$ K and 0.7×10^{11} K for the northern and southern lobes, respectively, and $\nu_{\rm m} \sim 1$ GHz. Higher $T_{\rm b}$ and lower $\nu_{\rm m}$ than those of NGC 1052 result in much lower B required from the SSA model for these sources.

Shaffer et al. (1999) claimed that the observed dependence of the apparent component separation of CTD 93 with wavelength is an additional evidence for SSA. NGC 1052 also shows such a frequency-dependence of the apparent component separation (see table 1), nevertheless, we mention that central condensation of the FFA opacities can explain it.

3.4. Free–Free Absorption Opacity Distribution

Applying a least-squares fit for the FFA spectrum at every image pixel, we obtain distribution of the FFA opacity $\tau_{\rm f}$, shown in figure 4a. The fit is applied for restored images at all three frequencies with a 3.0×1.5 mas beam in P.A.$= 0°$. The opacity map is clipped by the thresholds for the brightness of 5σ at 8.4 and 15.4 GHz. Pixels below 5σ at 2.3 GHz (and above 5σ at 8.4 and 15.4 GHz) are valid for the fit; we put the 5σ value as an upper limit. We reject pixels where the FFA fit does not result in a positive $\tau_{\rm f}$. The intrinsic spectral index α_0 is fixed to be -0.65 at every pixel, since three frequencies are insufficient to allow a freedom in α_0. It should be mentioned that the FFA opacity would be overestimated if α_0 were larger in the nucleus.

Figure 4b shows a slice of the distribution of the FFA opacities along the jet in P.A.$= 65°$. Error bars indicate formal errors of the least-squares fit for the FFA spectrum. The errors of registration between images at different frequencies, derived in section 3.1, can contribute to additional uncertainties

of the FFA opacities. To evaluate the uncertainties responding to the registration errors, we tentatively shifted images at 2.3 and 15.4 GHz relative to the 8.4-GHz image by 0.2 mas, performed the least-squares FFA fit, and then plotted the opacity profiles along the jet. Results of four test cases, with the shifts at 15.4 and 2.3 GHz, $(\delta\xi^{15.4}, \delta\xi^{2.3})$ of (+0.2, +0.2), (+0.2, −0.2), (−0.2, +0.2), (−0.2, −0.2) mas, are plotted in figure 5. The profiles align with that of the nominal registration, except a spike of $\tau_{\rm f} = 78$ at −2.7 mas from the nucleus in the case of $(\delta\xi^{15.4}, \delta\xi^{2.3}) = (-0.2, +0.2)$ mas. This spurious spike reflects on tolerance of the registration, where the brightness distribution holds a gap between components A and B. However, we have a small joint probability to meet such a bad case with opposite position errors for 2.3 and 15.4 GHz. We also attempted position shifts in the north–south direction, and confirmed that the opacity profile is insensitive in this direction, probably due to the elongation of the restoring beam.

As shown in equation 1, $\tau_{\rm f}$ can be used to investigate the cold dense plasma. The opacity peaks at $\tau_{\rm f} \sim 300$ towards the nucleus and decreases to the both downstreams. In the central sub-pc from the nucleus, we found a significant asymmetric distribution along the jet. The opacity falls rapidly at 0.1 pc in the eastern jet, while it smoothly decreases over 0.7 pc in the western jet. This feature can be seen in the trichromatic image (figure 2), in which blue color indicates opaque area at low frequency due to FFA. As stated before, we find that the eastern and western jets are approaching and receding, respectively, in the viewing angle of $\theta \sim 50°$. The dense absorber does not cover the approaching jet but does the receding jet. It implies that the absorber forms a disk or torus perpendicular to the jet as illustrated in figure 4c. In this configuration, the receding jet is covered with the torus but the approaching jet isn't. Rapid change of the opacity at 0.1 pc in the approaching jet suggests that the torus is geometrically thick with a thickness $H > r\cot\theta$, where r is the radius of the torus. Since the opacity tails along the receding jet up to ~ 0.7 pc from the nucleus, we consider that the radius of the torus is ~ 0.5 pc. The maximum opacity $\tau_{\rm f} = 300$ in the path length of ~ 0.7 pc gives a constraint for $n_{\rm e}$ and $T_{\rm e}$ by $n_{\rm e}^2 T_{\rm e}^{-1.5} = 930$. Ionization condition $T_{\rm e} > 10^4$ K constrains $n_{\rm e} > 3.1 \times 10^4$ cm^{-3}, then the column density $n_{\rm e}L \sim 0.7 \times 10^{23} (T_{\rm e}/10^4{\rm K})^{3/4}$ cm^{-2}. This is consistent with the atomic column density of $\sim 10^{23}$ cm^{-2} derived from the ROSAT and ASCA X-ray observations (Guainazzi, Antonelli 1999). Such a high column density is found via H I absorption towards some Seyfert and radio galaxies. Although H I column densities

hold an ambiguity of the spin temperature, $T_{\rm spin}$, those of $(3.9 \pm 0.5) \times 10^{21} (T_{\rm spin}/100\,{\rm K})$ cm^{-2} towards NGC 4151 (Mundell et al. 1995), $(2.54 \pm 0.44) \times 10^{19} T_{\rm spin}$ cm^{-2} towards Cygnus A (Conway, Blanco 1995), $14.0 \times 10^{21} (T_{\rm spin}/100\,{\rm K})$ cm^{-2} towards the core of Hydra A (Taylor 1996), $27.8 \times 10^{23} (T_{\rm spin}/8000\,{\rm K})$ cm^{-2} in the broad velocity-width component towards the core of PKS 2322−123 (Taylor et al. 1999), and $(19.3 \pm 3.8) \times 10^{21} (T_{\rm spin}/100\,{\rm K})$ cm^{-2} towards NGC 3079 (Sawada-Satoh et al. 2000) are comparable with electron column densities probed by FFA. Comparison of distribution of FFA with that of H I absorption could illustrate the ionizing surface of the torus.

3.5. Ambient Free–Free Absorbing Plasma

Besides the asymmetric condensation in the central 0.1 pc, the opacity widely extends in the outer region $x < -1.5$ mas in the approaching jet and $x > 10$ mas in the receding one. Here, x is the offset from the nucleus along the jet in P.A.= 65°. The opacity profile in this ambient absorber can be explained by the isothermal King model (King 1972):

$$n_{\rm e} = n_0 \left[1 + \left(\frac{r}{r_{\rm c}} \right)^2 \right]^{-1.5}, \tag{12}$$

where n_0 is the electron density at the centroid, r is the radius from the centroid and $r_{\rm c}$ is the core radius. Taking a least-squares fit for the opacities in $x < -1$ and $x > 4$ mas, we estimated $n_0 = (1.00 \pm 0.03) \times 10^4 (T_{\rm e}/10^4{\rm K})^{3/4}$ cm^{-3} and $r_{\rm c} = 0.84 \pm 0.02$ pc. The best-fit curve is shown as the green line in figures 4b and 6. See the Appendix for the analytic profile of the opacities towards the slant jets.

It is remarkable that the torus-like plasma distribution coexists with the spherically symmetric distribution. The former should be supported by the centrifugal force by rotation around the nucleus, while the latter is supported by the thermal pressure. We consider that our results witness the transition stage from the radial accretion to rotational accretion. We note that water masers (Claussen et al. 1998) distribute between components B and C, where the FFA torus covers foreground of the receding jet. Our results support the idea that the masers are amplified radio continuum emission from the receding jet by the foreground disk. The velocity gradient along the jet axis, faster receding velocity at closer position to the nucleus, may represent a dynamical infall in the torus.

4. Conclusion

We have performed trichromatic VLBA observations towards the nucleus of NGC 1052. Based on the peak frequency and brightness temperature, we identified the nucleus component in this object. Kinematics and orientation of the double-sided jets are derived from the Doppler beaming effect. We found that the spectra of the core and double-sided jets can be better fitted with the free–free absorption process by the cold dense plasma. Distribution of the opacity is biased towards the receding jet, suggesting a torus-like condensation perpendicular to the jet. Out of the torus, we also found an ambient plasma distribution which follows the spherical isothermal King model. Our results indicate the first look at a dynamical transition from the thermally-supported into centrifugally-supported in the subparsec-scale region of AGN.

We thank M. Miyoshi for helpful discussions. The VLBA is operated by the National Radio Astronomy Observatory, which is a facility of the National Science Foundation (NSF) operated under a cooperative agreement by Associated Universities, Inc. The Green Bank Interferometer is a facility of the NSF operated by the NRAO in support of NASA High Energy Astrophysics programs. This research has made use of data from the UMRAO which is supported by funds from the University of Michigan.

Appendix. FFA opacities along the plasma sphere with the isothermal King model

Here, we discuss about the optical depth of free–free absorption in the plasma sphere whose electron density follows the isothermal King model (King 1972). The model is derived from the force balance between the pressure gradient and self-gravity of the gas, assuming spherical symmetry and thermal equilibrium. The model gives the radial profile of particle density ρ as a function of the radius r by

$$\rho(r) = \rho_0 \left[1 + \left(\frac{r}{r_{\rm c}} \right)^2 \right]^{-\frac{3}{2}} . \tag{13}$$

Here, ρ_0 is the density at the center and $r_{\rm c}$ is the core radius. If we assume the isothermal condition in the relation between the electron density $n_{\rm e}$, the electron temperature $T_{\rm e}$, and the FFA opacity τ_0 will be

$$\begin{aligned}\tau_0 &= 0.46\int_{\rm LOS} T_{\rm e}^{-\frac{3}{2}} n_{\rm e}^2 dL \\ &= 0.46 T_{\rm e}^{-\frac{3}{2}} \int_{\rm LOS} n_{\rm e}^2 dL \\ &= 0.46 T_{\rm e}^{-\frac{3}{2}} n_{\rm e0}^2 \int_{\rm LOS} \left[1+\left(\frac{r}{r_{\rm c}}\right)^2\right]^{-3} dL. \end{aligned} \tag{14}$$

Here, $n_{\rm e0}$ is the electron density at the center in cm^{-3} and L is the path length along the line of sight in pc.

Let us consider the configuration as shown in figure 7. The integration of the optical depth in equation 14 should be taken from the jet at $\xi_0 = -\frac{x}{\tan\theta}$ to the infinity. The radius r from the nucleus is described in (x, ξ) coordinate as $r^2 = x^2 + \xi^2$. Therefore, equation 14 will be

$$\tau_0(x) = 0.46 T_{\rm e}^{-\frac{3}{2}} n_{\rm e0}^2 r_{\rm c}^6 \int_{\xi_0}^{\infty} (r_{\rm c}^2 + x^2 + \xi^2)^{-3} d\xi. \tag{15}$$

Here, we use the mathematical formula

$$\int (x^2+C)^{-3} dx = \frac{x}{4C(x^2+C)^2} + \frac{3x}{8C^2(x^2+C)} + \frac{3}{8C^2}\frac{1}{\sqrt{C}}\arctan\frac{x}{\sqrt{C}}, \tag{16}$$

where $C > 0$ is a constant. Equation 15 will be replaced as

$$\begin{aligned}\tau_0(x) = 0.46 T_{\rm e}^{-\frac{3}{2}} n_{\rm e0}^2 r_{\rm c}^6 \Bigg[&\frac{\xi_0}{4(r_{\rm c}^2+x^2)(\xi_0^2+r_{\rm c}^2+x^2)^2} + \frac{3\xi_0}{8(r_{\rm c}^2+x^2)^2(\xi_0^2+r_{\rm c}^2+x^2)} \\ &+ \frac{3}{8(r_{\rm c}^2+x^2)^2}\frac{1}{\sqrt{r_{\rm c}^2+x^2}}\left(\frac{\pi}{2} - \arctan\frac{\xi_0}{\sqrt{r_{\rm c}^2+x^2}}\right)\Bigg]. \end{aligned} \tag{17}$$

Let x replaced with a dimensionless quantity $x' = x/r_{\rm c}$, then equation 17 will be reduced as

$$\begin{aligned}\tau_0(x') = 0.46 T_{\rm e}^{-\frac{3}{2}} n_{\rm e0}^2 r_{\rm c} \Bigg[&\frac{x'}{4\tan\theta(1+x'^2)(1+\left(\frac{x'}{\sin\theta}\right)^2)^2} + \frac{3x'}{8\tan\theta(1+x'^2)^2(1+\left(\frac{x'}{\sin\theta}\right)^2)} \\ &+ \frac{3}{8(1+x'^2)^2\sqrt{1+x'^2}}\left(\frac{\pi}{2} - \arctan\frac{x'}{\tan\theta\sqrt{1+x'^2}}\right)\Bigg]. \end{aligned} \tag{18}$$

Figure 8 shows opacity profiles along the jets with different viewing angles, calculated by equation 18. As easily supposed, slant jet axis causes an asymmetric profile of the opacity. Since the electron density is larger towards the center, the opacity is larger within the core radius than outside. When the radiation source is far enough from the center, the opacity will be small at any given viewing angle.

References

Asada K., Kameno S., Inoue M., Shen Z.-Q., Horiuchi S., Gabuzda D. C. 2000, Astrophysical phenomena revealed by Space VLBI, H. Hirabayashi, P. G. Edwards, D. W. Murphy (ed), ISAS, Sagamihara, 51–54

Bicknell G. V., Dopita M. A., O'Dea C. P. 1997, ApJ 485, 112

Blandford R.D., Königl A. 1979, ApJ 232, 34

Claussen M.J., Diamond P.J., Braatz J.A., Wilson A.S., Henkel C. 1998, ApJL 500, L129

Conway J.E., Blanco P.R. 1995, ApJL 449, L131

de Vries W.H., Barthel P.D., O'Dea C.P. 1997, A&A 321, 105

Guainazzi M., Antonelli L.A. 1999, MNRAS 304, L15

Geldzahler B.J., Witzel A. 1981, AJ 86, 1306

Ho L.C., Filippenko A.V., Sargent W.L.W., Peng, C.Y. 1997, ApJS 112, 391

Jones D.L., Wehrle A.E., Meier D.L., Piner B.G. 2000, ApJ 534, 165

Kameno S., Horiuchi S., Shen Z.-Q., Inoue M., Kobayashi H., Hirabayashi H., Murata, Y. 2000, PASJ 52, 209

Kellermann K.I., Pauliny-Toth I.I.K. 1981, ARA&A 19, 373

Kellermann K.I., Vermeulen R.C., Zensus J.A., Cohen M.H. 1998, AJ 115, 1295

Kellermann K.I., Vermeulen R.C., Zensus J.A., Cohen M.H. 1999, BAAS 31, 856

King I.R. 1972 ApJL 174, L123

Knapp G.R., Gallagher J.S., Faber S.M. 1978 AJ 83, 139

Marr J.M., Taylor G.B., Crawford F. 2000, Astrophysical phenomena revealed by Space VLBI, H. Hirabayashi, P.G. Edwards, D.W. Murphy (eds), ISAS, Sagamihara, 91–94

Mundell C.G., Pedlar A., Baum S.A., O'Dea C.P., Gallimore J.F., Brinks E. 1995, MNRAS 272, 355

Mutel R.L., Hodges M.W., Phillips R.B. 1985, ApJ 290, 86

O'Dea C.P. 1998, PASP 110, 493

Pacholczyk A.G. 1970, Radio astrophysics, W.H. Freeman and company, San Francisco

Pearson T.J., Zensus J.A. 1987, Superluminal Radio Sources, ed. J.A. Zensus, T.J. Pearson, Cambridge University Press, Cambridge and New York

Shaffer D.B., Kellermann K.I., Cornwell T.J. 1999, ApJ 515, 558

Readhead A.C.S., Taylor G.B., Xu W., Pearson T.J., Wilkinson P.N., Polatidis A.G. 1996, ApJ 460, 612

Sawada-Satoh S., Inoue M., Shibata K.M., Kameno S., Migenes V., Nakai N., Diamond P.J. 2000, PASJ 52, 421

Taylor G.B. 1996, ApJ 470, 394

Taylor G.B., O'Dea C.P., Peck A.B., Koekemoer A.M. 1999, ApJL 512, L27

Vermeulen R.C., Readhead A.C.S., Backer D.C. 1994, ApJL 430, L41

Walker R.C., Romney J.D., Benson J.M. 1994, ApJL 430, L45

Walker R.C., Dhawan V., Romney J.D., Kellermann, K.I., Vermeulen R.C. 2000, ApJ 530, 233.

Table 1. Parameters of Gaussian components.

Comp.	Frequency (GHz)	Flux Density (mJy)	Relative R. A.[a] (mas)	Relative Dec.[a] (mas)	$\phi^b_{\rm maj}$ (mas)	$\phi^b_{\rm min}$ (mas)
A.....	2.274	969 ± 39	0	0	4.2	1.2
	8.424	1800 ± 130	0	0	3.4	0.9
	15.364	1310 ± 24	0	0	3.4	0.9
B.....	2.274	< 5.6	...	...	...	...
	8.424	77.0 ± 5.7	-4.59 ± 0.2	-2.03 ± 0.3	< 1.3	< 0.7
	15.364	488.7 ± 8.8	-3.59 ± 0.2	-1.36 ± 0.3	< 0.5	< 0.4
C.....	2.274	12.6 ± 2.2	-8.85 ± 0.7	-3.44 ± 1.8	2.1	1.4
	8.424	247.2 ± 18.0	-7.16 ± 0.2	-2.91 ± 0.3	1.6	0.6
	15.364	189.3 ± 3.8	-6.29 ± 0.2	-2.53 ± 0.3	1.6	0.6

[a]Relative position with respect to component A.

[b]Full width at half maximum (FWHM) of the major and minor axes of the Gaussian component.

Figure Captions

Fig. 1. Images of NGC 1052 at 2.3, 8.4, and 15.4 GHz, taken by use of the VLBA on 15 December 1998. Synthesized beam size (FWHM) are 6.06×2.45 mas in P.A.$= 3^\circ.92$, 2.01×0.78 mas in P.A.$= -1^\circ.91$, and 1.03×0.40 mas in P.A.$= -2^\circ.53$, shown in the left of each image. Contours start at $\pm 3\sigma$ level, increasing by factors of 2, where $\sigma = 1.246$, 2.277, and 0.823 mJy beam^{-1} for 2.3, 8.4, and 15.4 GHz, respectively.

Fig. 2. Trichromatic color image of NGC 1052 synthesized after we restore the images at 2.3, 8.4, and 15.4 GHz with a 3×1.5 mas beam, and register by referencing components A and C. Red, green, and blue color channels are allocated for the images at 2.3, 8.4, and 15.4 GHz, respectively. The origin of all images are referred by the position of component B, which is considered to be the nucleus. The blue part covering the nucleus and ~ 5 mas to the west indicates a steeply rising spectrum with $\alpha > 0$ due to large FFA opacities. Red color at both ends of the jets shows $\alpha < 0$, suggesting an optically-thin synchrotron emission.

Fig. 3. Spectra of components A, B, and C. The flux densities are measured by a Gaussian model fit using IMFIT in AIPS, as listed in table 1. The errors includes both formal errors and amplitude calibration errors. The solid lines for components A and C shows the best-fit FFA model $S_\nu = S_0 \nu^{\alpha_0} \exp(-\tau_{\rm f} \nu^{-2.1})$, where S_ν is the observed flux density in Jy, S_0 is the unabsorbed flux density at 1 GHz, α_0 is the intrinsic spectral index, $\tau_{\rm f}$ is the FFA opacity coefficient, and ν is the frequency in GHz.

Fig. 4. Distribution of the FFA opacity and a schematic model of a torus surrounding NGC 1052. (a): Distribution of FFA opacity $\tau_{\rm f}$ is drawn in grey scale. The opacity is calculated by the least-squares fit for the FFA model $S_\nu \propto \nu^{\alpha_0} \exp(-\tau_{\rm f} \nu^{-2.1})$. It is obtained by the trichromatic image (figure 2), which is restored with a 3×1.5 mas beam. The fit is applied at pixels of 0.1×0.1 mas with the thresholds for the brightness of 5σ at 8.4 and 15.4 GHz. Pixels below 5σ at 2.3 GHz (and above 5σ at 8.4 and 15.4 GHz) are valid for the fit; we put the 5σ value as an upper limit. We clipped out pixels where the FFA fit does not result in a positive $\tau_{\rm f}$. (b): The opacity profile along the jet in

P.A.= 65°. It peaks $\tau_{\rm f} \sim 300$ at the nucleus. It tails over ~ 0.7 pc along the western (receding) jet, and rapidly falls at 0.1 pc in the eastern (approaching) jet. Out of this region, an extended profile of an ambient FFA absorber can be seen. The green curve shows the best-fit model of the FFA opacity by the ambient plasma with the isothermal King model distribution $n_{\rm e} = n_0 \left[1 + \left(\frac{r}{r_{\rm c}}\right)^2\right]^{-1.5}$. (c): A schematic diagram of NGC 1052. The nucleus and the double-sided jets are visible at 15.4 GHz, with the viewing angle of 50°. The ambient plasma (green) distributes around the nucleus supported by its thermal pressure, which contributes an extended FFA components. The FFA torus is presumed to lie perpendicular to the double-sided jets. It covers ~ 0.7 pc of the receding jet and ~ 0.1 pc of the jet, to generate the asymmetry seen in the opacity distribution.

Fig. 5. Tolerance of the FFA opacity profile along the jet against position errors in registration. The thick line is the same with figure 4b, which shows the opacity profile with nominal registration. The thin lines represents results of four test cases, with the shifts at 15.4 and 2.3 GHz, $(\delta\xi^{15.4}, \delta\xi^{2.3})$ of (+0.2, +0.2), (+0.2, −0.2), (−0.2, +0.2), (−0.2, −0.2) mas. These tentative profiles align with that of the nominal registration, representing the peak towards the nucleus, the tail to the west receding jet, and the break at 1 mas to the east approaching jet. A spike of $\tau_{\rm f} = 78$ at −2.7 mas from the nucleus can be seen only in the case of $(\delta\xi^{15.4}, \delta\xi^{2.3}) = (-0.2, +0.2)$ mas, which reflects on tolerance of the registration when we have opposite registration errors for 2.3 and 15.4 GHz.

Fig. 6. The FFA opacities of NGC 1052 out of the torus. The horizontal axis indicate the offset along the jet in P.A.= 65° in pc, where 1 mas corresponds to 0.1 pc. Negative and positive offsets stand for eastern (approaching) and western (receding) jets, respectively. The vertical axis shows the free–free absorption coefficient $\tau_{\rm f}$ derived from the FFA model fit. Opacities in the torus $-1 < x < 4$ mas (or -0.1 to 0.4 pc) are removed from the plot. The solid grey line shows the opacity calculated from the isothermal King model, which is calculated in the Appendix and shown in figure 6. Here we take the viewing angle $\theta = 50°$. The best fit gives $n_0 = (1.00 \pm 0.03) \times 10^4 (T_{\rm e}/10^4{\rm K})^{3/4}$ cm^{-3} and $r_{\rm c} = 0.84 \pm 0.02$ pc.

Fig. 7. The FFA optical depth towards the twin jets along the plasma with the density profile of the

isothermal King model. Let the z and x axes be parallel and perpendicular to the line of sight, respectively, and let the nucleus be the origin. The jet, as a synchrotron emitter, is inclined from the line of sight by the viewing angle θ. The opacity integration, as a function of x, is taken from the jet at $z_0 = -\frac{x}{\tan\theta}$ to the infinity.

Fig. 8. Profiles of the FFA optical depth towards the jets with different viewing angles. The horizontal axis is the offset along the jet in unit of the core radius $r_{\rm c}$. Negative offset stands for the approaching jet side. The vertical axis is the normalized opacity, when $T_{\rm e}^{-\frac{3}{2}} n_{\rm e0}^2 r_{\rm c}$ is unity.

Fig. 1

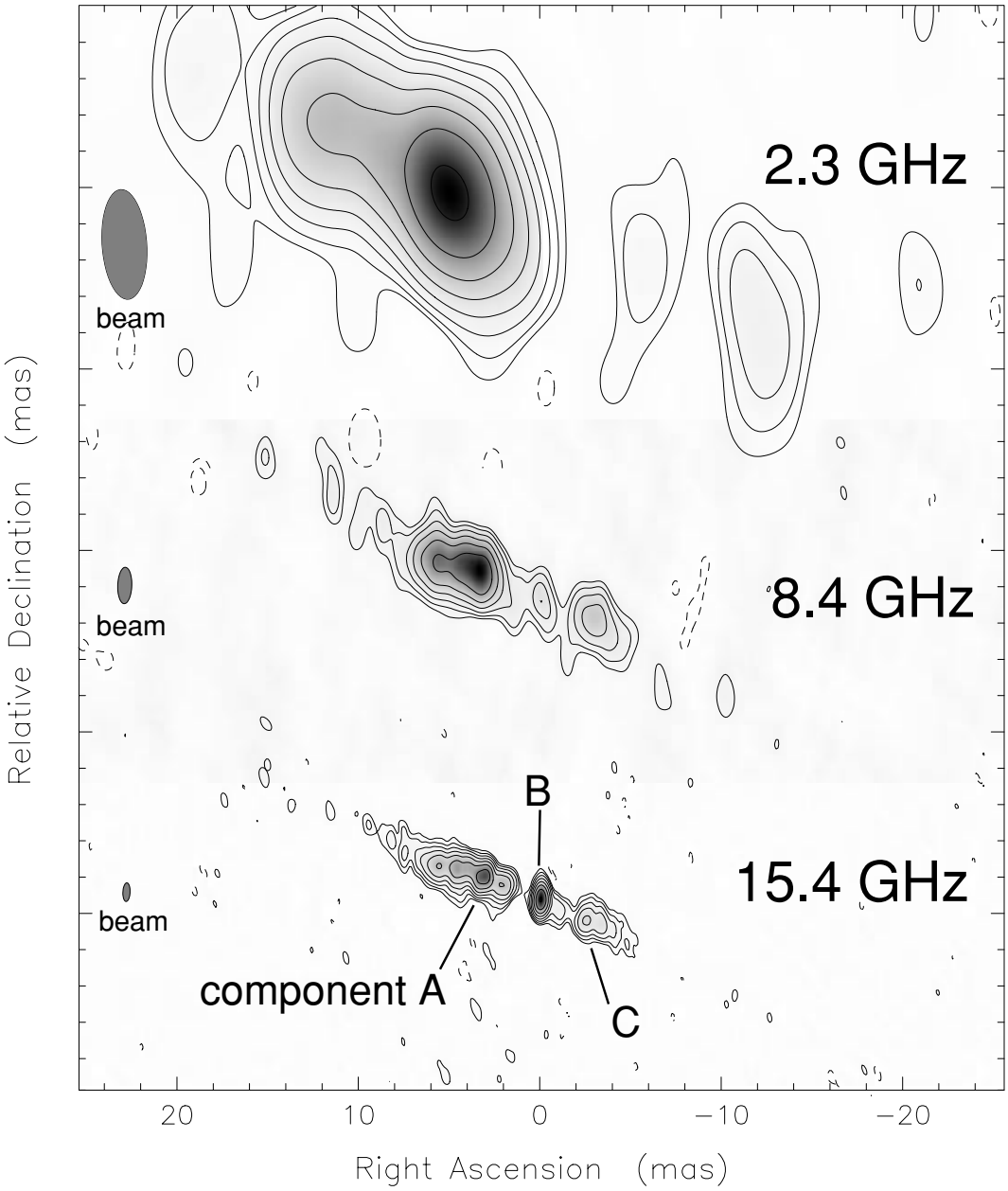
2.3 GHz
beam
8.4 GHz
beam
15.4 GHz
beam
B
component A
C
Relative Declination (mas)
Right Ascension (mas)
20
10
0
−10
−20

Fig. 2

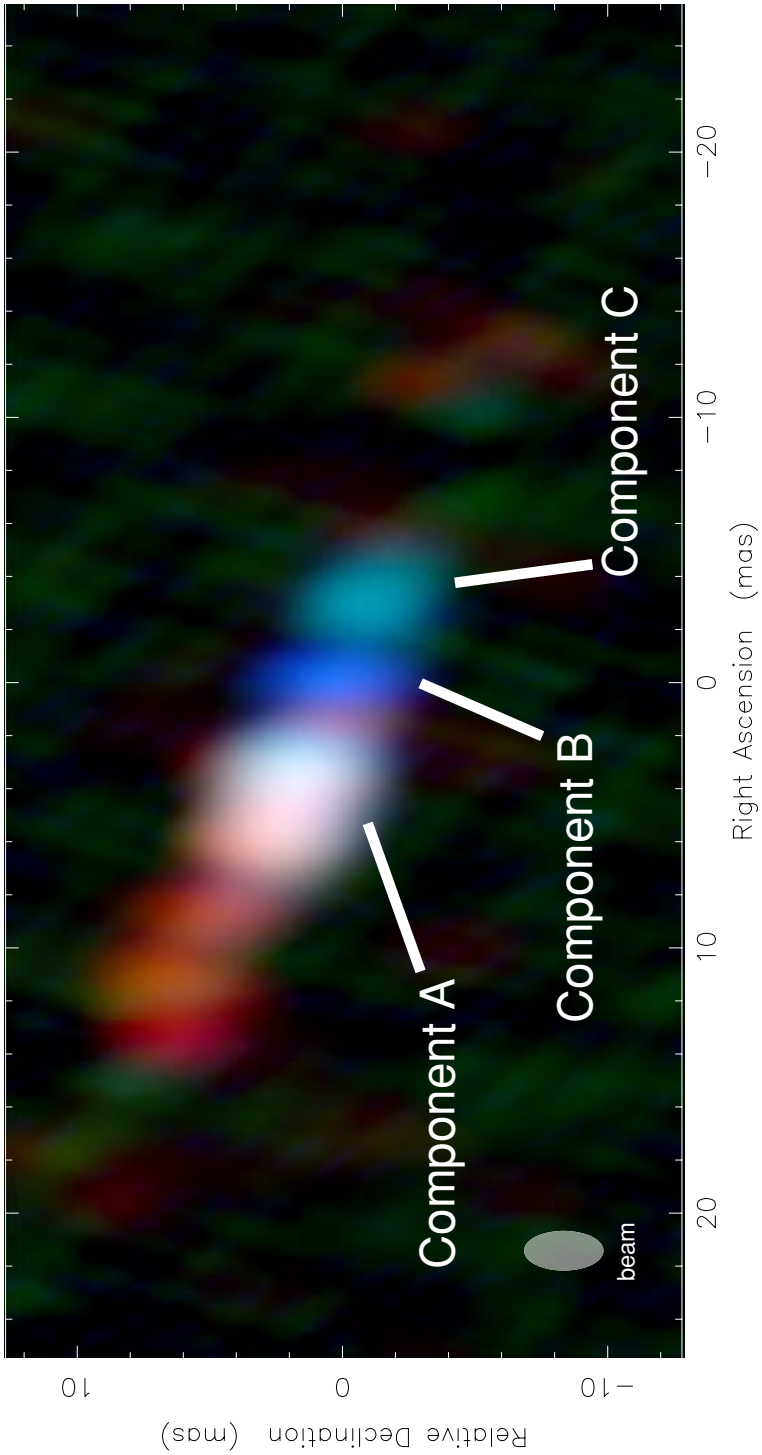
Component A
Component B
Component C
beam
20
10
0
−10
−20
Right Ascension (mas)
10
0
−10
Relative Declination (mas)

Fig. 3

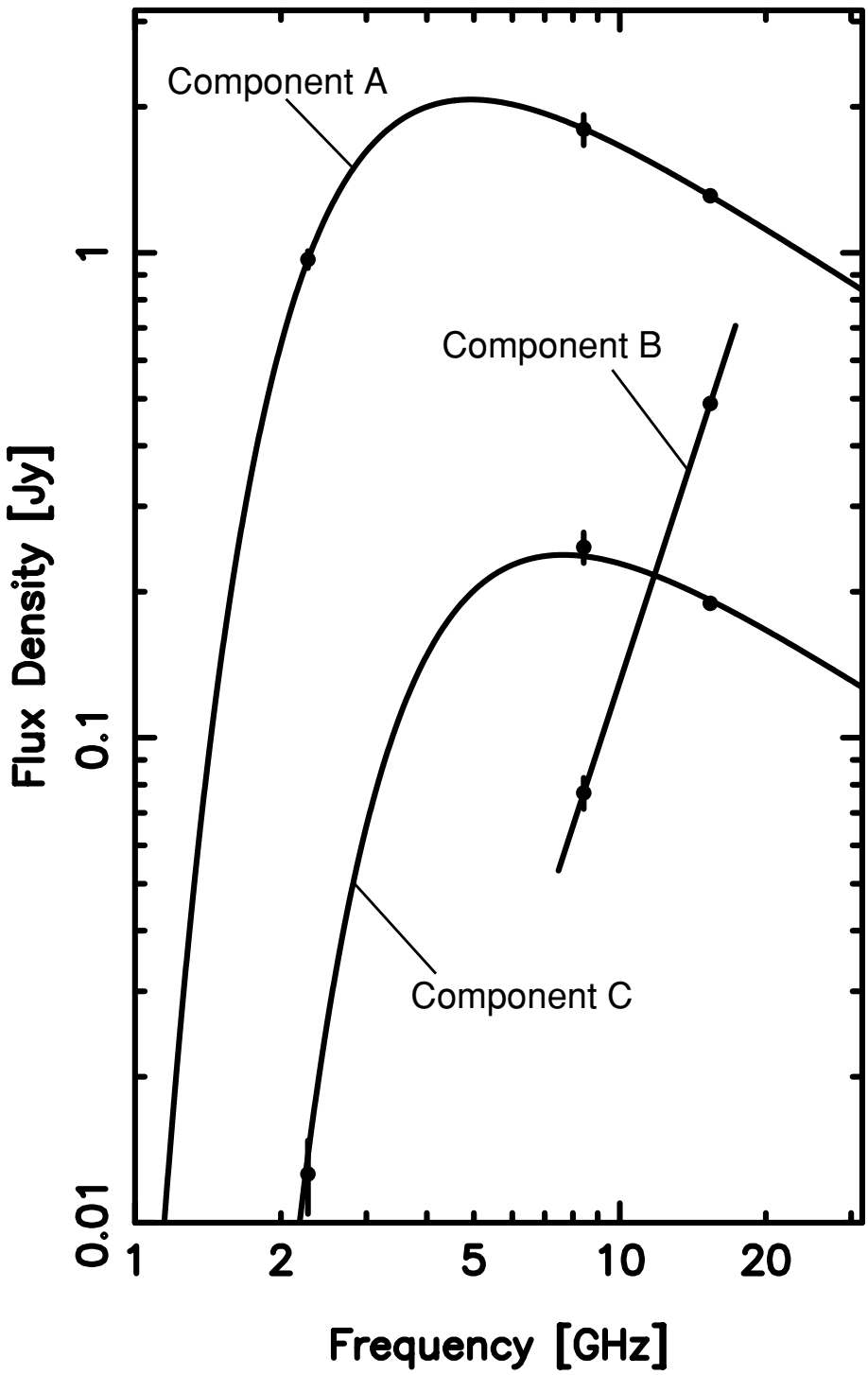
Component A
Component B
Component C
Flux Density [Jy]
1
0.1
0.01
1
2
5
10
20
Frequency [GHz]

Fig. 4

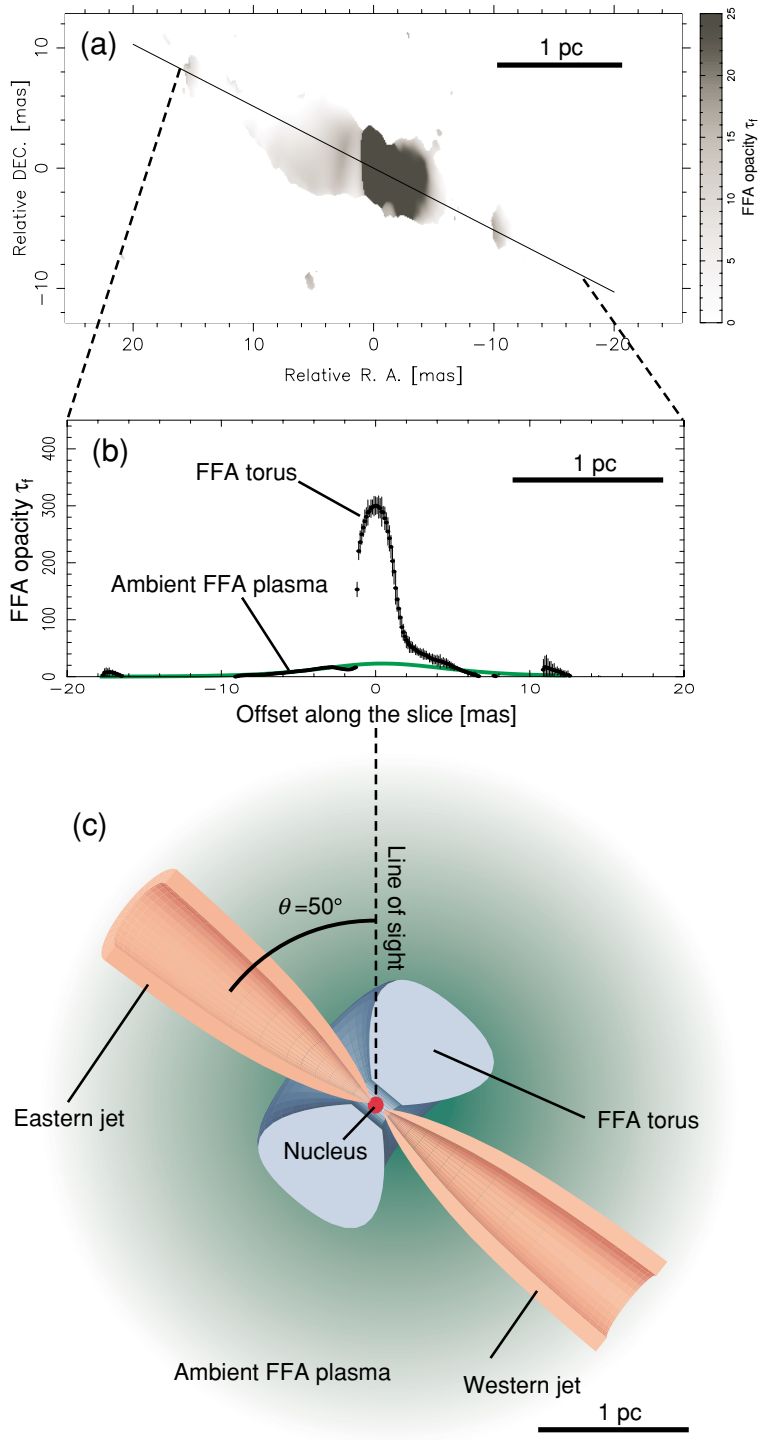
(a)
1 pc
Relative DEC. [mas]
Relative R. A. [mas]
FFA opacity τ_f
(b)
FFA torus
1 pc
Ambient FFA plasma
FFA opacity τ_f
Offset along the slice [mas]
(c)
θ =50°
Line of sight
Eastern jet
FFA torus
Nucleus
Ambient FFA plasma
Western jet
1 pc

Fig. 5

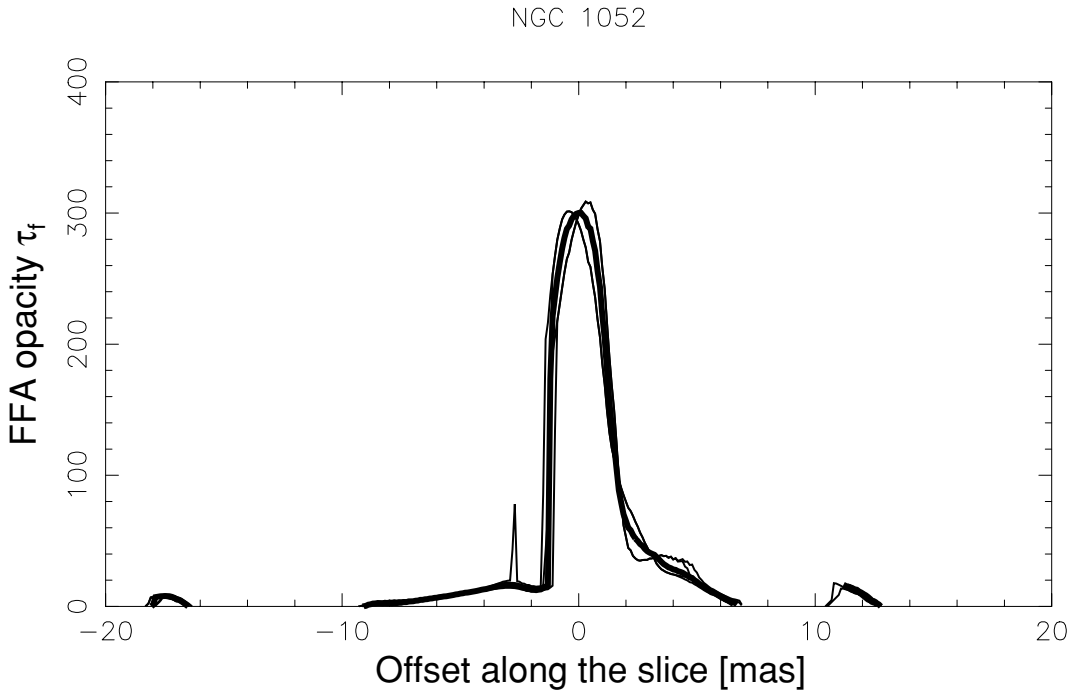
NGC 1052
FFA opacity τ_f
0
100
200
300
400
−20
−10
0
10
20
Offset along the slice [mas]

Fig. 6

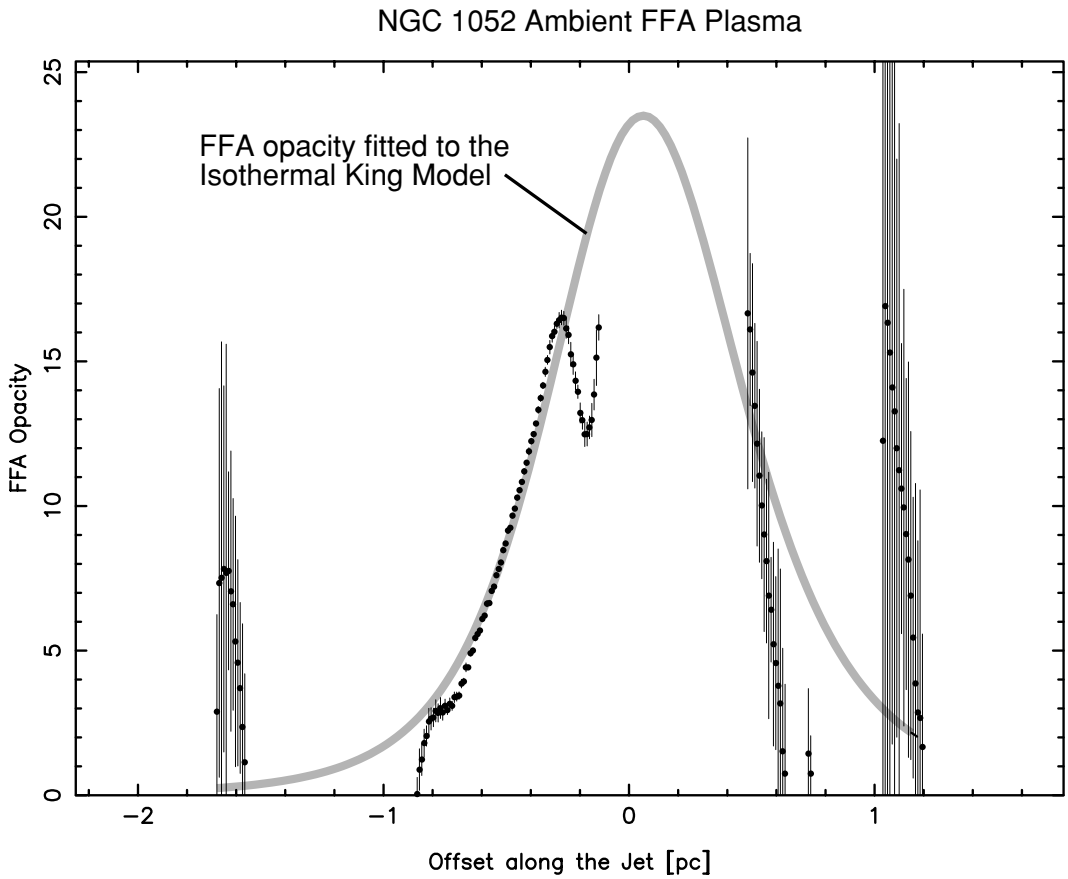
NGC 1052 Ambient FFA Plasma
FFA opacity fitted to the
Isothermal King Model
FFA Opacity
Offset along the Jet [pc]
0
5
10
15
20
25
−2
−1
0
1

Fig. 7

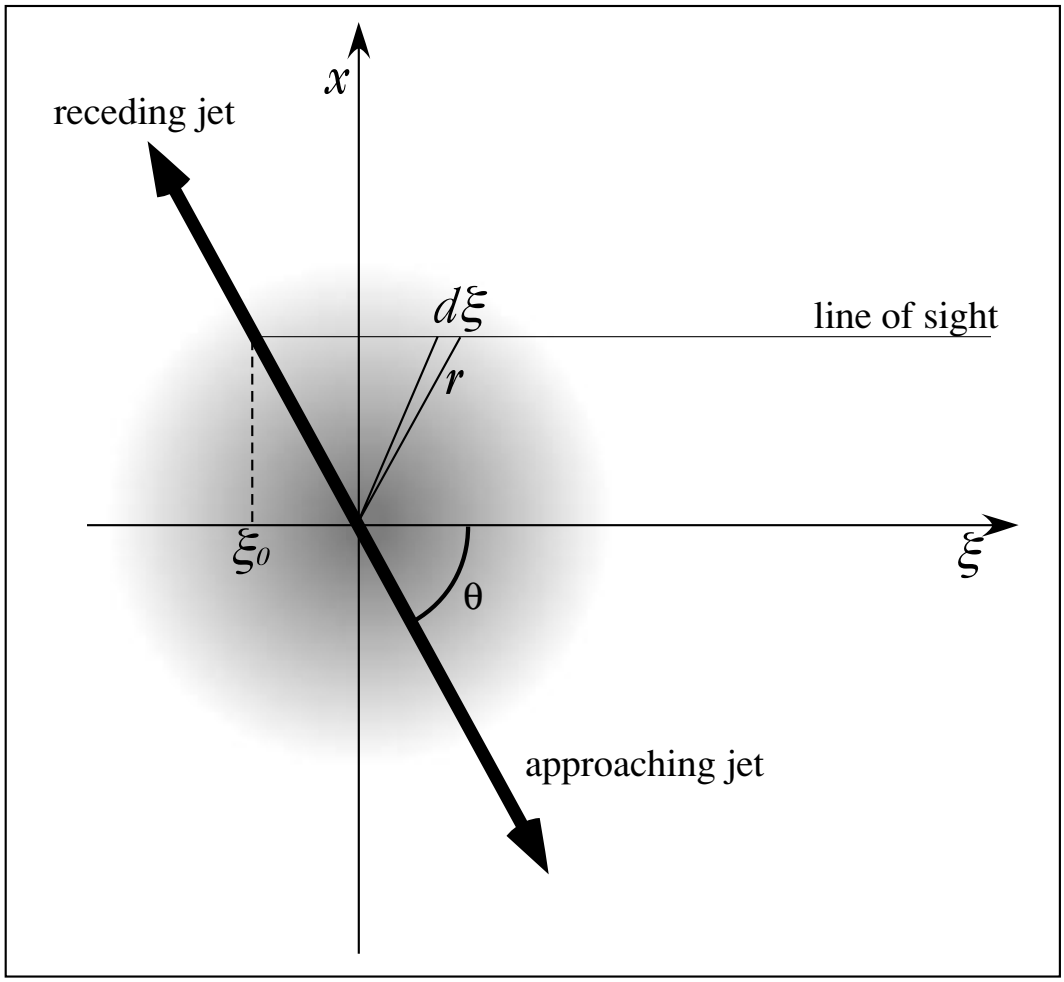

Fig. 8

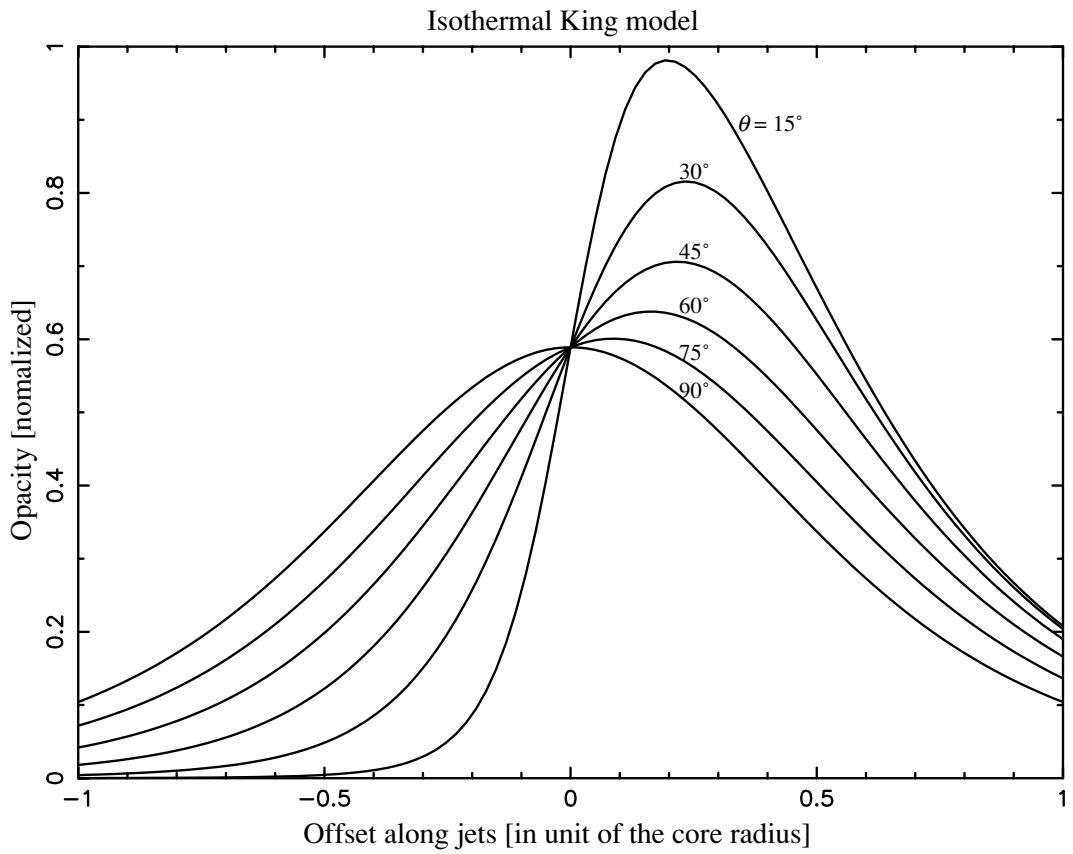
Isothermal King model
θ = 15°
30°
45°
60°
75°
90°
Opacity [nomalized]
0
0.2
0.4
0.6
0.8
1
−1
−0.5
0
0.5
1
Offset along jets [in unit of the core radius]